nature geoscience

Supplementary information

https://doi.org/10.1038/s41561-025-01797-y

Deep mantle heterogeneities formed through a basal magma ocean contaminated by core exsolution

In the format provided by the authors and unedited

Table of contents:

Supplementary Discussion 1: Size of core exsolution crystallite

Supplementary Discussion 2: Dissolution rate

Supplementary Discussion 3: Initial composition and thickness of the basal magma ocean

Supplementary Discussion 4: Comparison with alternative thermodynamic models

Supplementary Discussion 5: Exsolution rate of MgO and SiO_2

Supplementary Discussion 6: Effects of initial thickness of BMO and exsolution rate

Supplementary Discussion 7: Si isotope composition of the core exsolution

Supplementary Discussion 8: Mixing model

Supplementary Fig. 1: Density difference ($\Delta\rho$) between exsolution and the PREM

Supplementary Fig. 2: Density profile of the eight layers in the lowermost BECMO mantle

Supplementary Fig. 3: Viscosity profile of the reference BECMO mantle after 4.5 Gyr

Supplementary Fig. 4: Si isotopic composition of SiO_2 exsolution $\delta^{30}Si_{SiO2}$.

Supplementary Table 1. Mixing model inputs.

Supplementary Discussion 1: Size of core exsolution crystallite

Exsolution occur when concentrations of light elements in the core reach the supersaturation limit during the cooling process. The core exsolution crystallite size can be determined based on two key considerations. First, thermodynamic constraints dictate that the size of an exsolution must exceed the critical nucleus size to ensure its stable existence. Second, the buoyancy of the exsolution must overcome convective stirring in order for it to rise and ascend into the mantle.

For both homogeneous and heterogeneous nucleation, the critical nucleus size is

$$d_{nuc} = \frac{2\sigma}{\Delta G}, \quad \text{(S1)}$$

where σ is the interfacial energy between the oxides and core fluid; ΔG the Gibbs free energy difference between the liquid and solid phases of the exsolution per volume. The interfacial energies at the conditions of the outer core are not well-known. At 1 bar, interfacial energies are approximately 1.8 Jm^{-2} for solid MgO/molten steel[1] and 1.6 Jm^{-2} for solid SiO_2/liquid iron[2,3], respectively. ΔG can be estimated using the thermodynamic database[4]. The resulting critical nucleus sizes are approximately 3 nm and 0.5 nm for MgO and SiO_2 crystals, respectively.

The outer core vigorously convects. Although MgO and SiO_2 are buoyant in the outer core, the strong convective motion may entrain exsolved core materials if convective entrainment outweighs gravitational force. Here we estimate the critical size of exsolution above which crystals would sediment towards the CMB by[5]

$$d_{sed} = \left(\frac{\eta_c \alpha g F}{C_p}\right)^{1/2} \frac{1}{\Delta\rho_c g Sh}, \quad \text{(S2)}$$

where α, η_c, C_p are the thermal expansion coefficient (2×10^{-5} K^{-1}) [6], viscosity (0.01 Pa s)[7], and isobaric heat capacity (800 J kg^{-1} K^{-1})[6] of the outer core fluid, respectively; F (164 mW m^{-2}) the heat flux across the CMB [8]; g (10 m s^{-2}) the gravitational acceleration; $\Delta\rho$ (~5 g/cm^3) is the density difference between the core fluid and precipitation[9,10]. Sh is the non-dimensional Shields number, defined as the ratio of the tangential stress from convective flow over the buoyancy stress relative to the density difference between the crystals and the melt. When Sh is below 0.1-0.2, sedimentation occurs[5]. The critical radius separating sedimentation and entrainment is around 2 nm. In other words, MgO will sediment immediately after exsolution, and SiO_2 will grow to around 2 nm until sedimentation.

In summary, the critical nucleus sizes (d_{nuc}) are of the same order of magnitude as the critical sizes that separate entrainment and sedimentation (d_{sed}). Therefore, the MgO and SiO_2 exsolution, upon nucleation to form nanoparticles, will rapidly sediment and ascend into the overlying magma ocean.

Supplementary Discussion 2: Dissolution rate

Crystal dissolution in silicate melts is a critical igneous process that has been well studied both experimentally and theoretically. Note that dissolution is driven by the chemical gradient of solute and can be efficient even at temperatures below the melting point of crystal[11]. Here, we focus on the case of convective dissolution where a single spherical oxide exsolution crystal of diameter d rise in an infinite reservoir of melt driven by buoyancy[11]. The crystal dissolution rate is,

$$u = \frac{\beta D}{\delta}, \tag{S3}$$

where D (~10^{-9} m^2 s^{-1}) is the diffusivity of components of interest in the melt[12]; β a dimensionless parameter defined as

$$\beta = \frac{\rho_m (C_0 - C_\infty)}{\rho_{\mathrm{ex}} (C_{\mathrm{ex}} - C_0)}, \tag{S5}$$

and δ the effective boundary layer thickness by

$$\delta = \frac{d}{2 + 0.6 (\frac{g d^3 \Delta\rho_m}{\eta_m D})^{1/4}}, \tag{S4}$$

where ρ_m/ρ_{ex} is the density of melt/exsolution in the magma ocean. C_{ex} is the concentration of component of interest in the exsolution. We set C_{ex} = 0.9 as precipitation is relatively pure SiO_2 seifertite and (Mg,Fe)O ferropericlase[10,13]. C_0 corresponds to the equilibrium-determining component at the interface and is assumed to be 0.7[4,14]. C_∞ represents the concentration of component far away from the exsolution and evolves moderately with solidification (Fig. 2). For simplicity, we set C_∞ to 0.5 in our analysis. $\Delta\rho_m$ is the density difference between the silicate melts and exsolved core material (Supplementary Fig. 1). η_m (0.1 Pa s) is the viscosity of silicate melts[12]. The resulting dissolution rate is shown in Extended Data Fig. 1.

Supplementary Discussion 3: Initial composition and thickness of the basal magma ocean

The basal magma ocean (BMO) emerges as an inevitable consequence of the magma ocean solidification regardless of the depths of onset of solidification, mainly owing to the strong partitioning of Fe into the silicate melts at high pressures[15]. A BMO forms when the deep magma ocean is separated from the overlying mantle by a rheologically solid layer. The initial thickness of the BMO is thus sensitive to the location of this layer, which in turn is governed by many factors such as the melt-solid density crossover, grain size, and critical melt fraction for rheological transition. However, these factors are generally poorly constrained. As such, the initial BMO thickness remains an open question and a wide range of thickness has been considered in the literature, such as 1000 km [8], 750 km[16], 400 km[17], and 150 km[18].

Here, we consider the initial thickness and composition of the BMO based on a scenario where the downward percolation of residual melt from a rheologically solid (mushy) layer creates a layer above the CMB. We set the initial CMB temperature in our model to 4900 K. This CMB temperature, assuming an adiabatic temperature profile in a magma ocean, would yield a solid-melt density crossover pressure of 80-115 GPa from the model of ref.[17], suggesting that residual melt below 80-115 GPa would be transported toward the CMB. Considering that the initial core was about 200 km thicker than it is today, the initial thickness of the BMO was 150-800 km. It is, however, noted that not all residual melts would end up in the BMO, as some may solidify within the mushy layer due to its rapid cooling, which would further reduce the initial thickness of the BMO.

Supplementary Discussion 4: Comparison with alternative thermodynamic models

The density profile of the solidified BECMO mantle is sensitive to the choice of the thermodynamic model[4,14,19-21]. For example, the model by ref. [14] exhibits a significantly smaller bridgmanite stability field within the ternary phase diagram. In our phase diagram (Extended Data Fig. 2), the SiO_2 ratio along the cotectic line of bridgmanite + ferropericlase is lower compared to ref. [14], especially in the FeO-enriched domain. This discrepancy arises from differences in the Fe partitioning between melt and ferropericlase. Our model incorporates updated experimental constraints from refs. [22-24], which report an order of magnitude smaller mineral-melt partition coefficients of iron than those in ref. [14]. The difference in the phase diagram leads to distinct model predictions. At the initial stage, both models predict the exsolution of bridgmanite. However, due to the differences in cotectic composition, our model predicts a longer residence time in the bridgmanite-stability field (brg-field). In the case of a no-exsolution BMO, our model predicts that the melt composition reaches the cotectic line at a much more Fe-rich and Si-poor composition compared to ref. [14]. As crystallization proceeds along the MgO-$MgSiO_3$ cotectic valley, this model procudecs a larger amont of ferropericlase than ref. [14]. For the scenario of BECMO, as the melt composition approaches the cotectic line, it begins to evolve nearly parallel to this line. This trajectory is the combined effects of (1) the exsolution of MgO and SiO_2 (shown by the green vector) and (2) the removal of bridgmanite ($(Mg_{1-x},Fe_x)SiO_3$, where x is small; shown by the orange vector). The first effect becomes increasingly significant as the BMO thins and becomes enriched in iron, which in turn slows the rate of solidification. The added vector points in a direction that delays the approach to the cotectic line, keeping the BECMO composition within the brg-field, until it eventually converges with the cotectic line of $MgSiO_3$-SiO_2, crystallization of bridgmanite and seifertite is predicted at this stage, but we note that the model is not well calibrated for SiO_2-rich compositions due to the lack of experimental datas, and constraining the actual seifertite content will require further investigation. Nevertheless, the cyrstalization of seifertite is likely, which would delay the cyrstalizallization of ferropericlase at the lowermost mantle. Additionally, the adopted model predicts larger changes in liquidus temperature within the brg-field, resulting in a larger amount of exsolution during a given thickness of BMO solidification. By contrast, ref. [14] will yield the cyrstlization of bridgmanite and ferropericlase at an earlier stage due to the smaller area of bridgmanite stability field, and a shallower liquidus temperature gradient. In addition, the slope of the liquidus bridgmanite liquidus controls the amount of bridgmanite crystalized per degree of cooling, and therefore also determine the amount of exsolution needed to replenish the SiO_2 consumed. We note that the thermodynamic model used in this study exhibits a steeper liquidus slope than that in ref. [14], which likely results in a more silica-enriched mantle composition for BECMO.

Nevertheless, no thermodynamic model fully reconciles all existing high-pressure experimental constraints, including melting temperature, density, and partitioning coefficients, which have been extensively studied over the last decade. For example, MgO-$MgSiO_3$ eutectic compositions predicted by ref. [14], although in reasonable agreement with the experiments by ref. [21], contradicts the high-pressure experiments by ref. [20]. Regardless of the model used, the issue of a large fraction of dense, FeO-rich cumulates in the lowermost solidified BMO likely persists, as noted in ref. [25]. We do not intend to present our results as a definitive answer; rather, we aim to demonstrate a proof of concept for the BECMO hypothesis. Furthermore, the results are sensitive to the initial BMO thickness and the exsolution rate. For example, in our study, a lower exsolution rate would result in the BECMO composition intersecting the cotectic line at a shallower depth than shown in (Extended Data Fig. 9). These uncertainties suggest multiple possibilities for the mineralogical structure of the post-solidification mantle during the Hadean. More extensive studies are warranted to further address and elucidate these uncertainties.

Supplementary Discussion 5: Exsolution rate of MgO and SiO_2

The exsolution rate is given by dc/dT, where c is the oxide (i.e., MgO, SiO_2) component content in the core and T is temperature. Exsolution rate and exsolution species depend on the initial composition of the core[10,26], which is subjected to large uncertainties. For a reasonable range of initial core compositions, the exsolution rate of SiO_2 may vary between 4.1×10^{-5} and 14×10^{-5} K^{-1} [27], and that of MgO between 1×10^{-6} K^{-1} and 1×10^{-5} K^{-1} [26,28,29]. We test the geodynamic consequences of exsolution rates. Generally, a large exsolution rate leads to FeO-diluted BECMO, weak enrichment of FeO in the lowermost mantle, and thus thin, dense piles structures. In contrast, a small rate favors strong enrichment of FeO in the lowermost mantle, resulting in thick, persistent layers. The effects of exsolution rate are offset by the initial thickness of the BMO.

Here we adopt a constant SiO_2 exsolution rate of 7.3×10^{-5} K^{-1} [27]and a temperature-dependent MgO exsolution rate following ref. [30], while acknowledging that a systematic analysis on the trade-off between exsolution rate and the initial BMO thickness is warranted. These exsolution rates correspond to 8 wt% SiO_2 exsolution and 0.4 wt% MgO assuming a CMB temperature drop of around 1000 K, as considered here. In other words, we assume that the core at least contains 3.4 wt% Si, 4.2 w% O, and 0.51 wt% Mg initially, which align with previous estimates[31,32].

Supplementary Discussion 6: Effects of initial thickness of BMO and exsolution rate

The dissolution of iron-poor exsolution products from the core into the BMO dilutes the FeO concentration of the BMO, thereby suppressing the formation of a thick FeO-rich layer. The effectiveness of such dilution hinges on two factors: the exsolution rate, and the BMO volume (or equivalently, its initial thickness). Thermodynamic modeling across various exsolution rates and initial BMO thicknesses reveals a clear trade-off between these parameters (Extended Data Fig. 9). A thick initial BMO and a low exsolution rate would lead to small degree of dilution, whereas a thin BMO and a large exsolution rate promote strong dilution. This trade-off remains valid despite pressure-induced shifts in the ternary phase diagram, as Mg-rich bridgmanite consistently serves as the liquidus phase across a wide compositional range in the deep mantle. Given a SiO_2 exsolution rate of 8×10^{-5} K^{-1}, doubling the initial BMO thickness increases the bottom density of the solidified BECMO by approximately 400-700 kg m^{-3}. Similarly, for a given initial BMO thickness of 350 km, a lower SiO_2 exsolution rate leads to less SiO_2 addition, resulting in a higher bottom density and concurrently a thinner solidified BECMO mantle. If a density profile with a bottom density exceeding 6020 kg m^{-3} cannot generate the present-day mantle structures and the BECMO model fails, then the maximum allowable BMO thickness are approximately 350 km and 250 km for SiO_2 exsolution rates of 8×10^{-5} and 2×10^{-5}, respectively. We define a new parameter, the normalized exsolution rate, as the product of the exsolution rate and the core mass, divided by the initial BMO mass. As expected, increasing the normalized exsolution rate reduces the bottom density.

Supplementary Discussion 7: Si isotope composition of the core exsolution

We consider two steps of Si isotope fractionation: the first is the silicate-metal fractionation during the core formation at temperature $T_{\text{core\_formation}}$, and the second is the SiO_2-metal fractionation during the exsolution at temperature $T_{\text{exsolution}}$. In both cases, the light Si isotope preferentially fractionates into the metallic phase, although the degree of fractionation is still controversial[33-36].

The metal-silicate fractionation factor is denoted as $\Delta^{30}\text{Si}$ with $\Delta^{30}\text{Si} = \delta^{30}\text{Si}_{silicate} - \delta^{30}\text{Si}_{metal}$ and $\delta^{30}\text{Si} = [\frac{(^{30}\text{Si}/^{28}\text{Si})_{\text{sample}}}{(^{30}\text{Si}/^{28}\text{Si})_{\text{reference}}} - 1] \times 1000$. We assume that the experimentally determined metal-silicate fractionation factors apply to both steps, and consider two endmember cases of $\Delta^{30}\text{Si} = \text{k}/T^2$, where T is temperate and k is the fractionation constant, i.e., 7.6×10^6 [35] or 4.4×10^6 [34]. Both k values are considered in this study. It should be noted that in our assumptions, Si isotope fractionation is solely temperature sensitive and independent of pressure[31]. Assuming that the core fluids equilibrate with the bulk silicate Earth (BSE) ($\delta^{30}\text{Si}_{BSE}$= –0.29±0.07‰)[37,38], the final Si isotope composition of the SiO_2 exsolution can be expressed as:

$$\delta^{30}\text{Si}_{SiO2} = \delta^{30}\text{Si}_{BSE} - \text{k}\left(\frac{1}{T_{\text{core\_formation}}^{\ 2}} - \frac{1}{T_{\text{exsolution}}^{\ 2}}\right) \quad \text{(S5)}$$

Here we adopt a single stage core formation temperature of 3350 K[31] and set $T_{\text{exsolution}}$ as the CMB temperature, which decreases from 5000 K to 3600 K over the past 4.5 billion years. The results are shown in Supplementary Fig. 4. We note that a lower core formation temperature would cause a stronger negative Si isotope anomaly in exsolved SiO_2.

Supplementary Discussion 8: Mixing model

We model the mixing of core exsolution products with the overlying mantle materials. Based on previous studies[39,40], we assume that the isotopic signatures of W and He remain unaffected by the solid-solid phase transition and partial melting and ignore the potential pressure-dependent isotope fractionation during the upwelling of deep mantle materials. Various mantle components may exist. Here we consider four mantle components in the framework of our BECMO model, including the ambient mantle, dense piles, and two core exsolution products with different W metal-oxide partition coefficients (D_W). The ambient mantle material is assumed to have a $^3He/^4He$ ratio of 8 R_A where $R_A = 1.384\times10^{-6}$ [41] and $\mu^{182}W$ of 0. The element partitioning depends on the system and physical conditions, and likely varies with temperature and the chemistry of exsolution. Nevertheless, following ref. [9], we set the metal-oxide partition coefficient of helium D_{He} =0.06 for simplicity. Unfortunately, there are no data on W partitioning between core fluid and the exsolution (D_W) at the CMB conditions. We consider both D_W =1 (Exsolution 1), based on the preliminary experimental results [42] and D_W =10 (Exsolution 2) based on the metal-silicate partitioning experiments[43]. We assume that exsolution inherits the isotopic composition of the core fluid with $^3He/^4He$ ratio of 120 R_A [44], and $\mu^{182}W$ of –220. The W and He concentrations in the core are 470 ppb [45] and 3.36 ppb [46], respectively. The elemental and isotopic composition of the mantle after solidification BECMO is calculated self-consistently and the results are presented in Fig. 2 for the addition of Exsolution 1 only. Geodynamic simulations shows that the entrainment of dense piles becomes increasingly difficult with the depth. Essentially, only those dense pile materials that are formed above 2810 km can be effectively entrained (Supplementary Fig. 2). As W and He compositions of the solidified BECMO mantle at these depths only vary slightly, we take their averages as the inputs for the dense pile. The detailed model inputs of all four mantle components are summarized at Supplementary Table. 1.

The distinct isotopic signature of OIBs is the anticorrelation of the $^3He/^4He$ ratio and $\mu^{182}W$. In the framework of our BECMO model, only two components yield such a feature – the core exsolution products and solidified BECMO mantle. Therefore, either of these materials or both must be included in order to reproduce the observations. We consider two different mixing scenarios: the mixing between Exsolution 1, Exsolution 2, and the ambient mantle (Extended Data Fig. 10a), and between the dense pile, Exsolution 2, and ambient mantle (Extended Data Fig. 10b).

Here we adopt the $\mu^{182}W$ and W concentration of the ambient mantle from ref. [47]. These values, as well as those of other mantle reservoirs, are subject to refinement. Notably, recent studies have proposed slightly revised $\mu^{182}W$ and W concentrations[48,49]. While the specific proportions of components required in the mixing model may shift accordingly, the ability of our mixing models to reproduce the observed $\mu^{182}W$–$^3He/^4He$ anti-correlation remains unchanged.

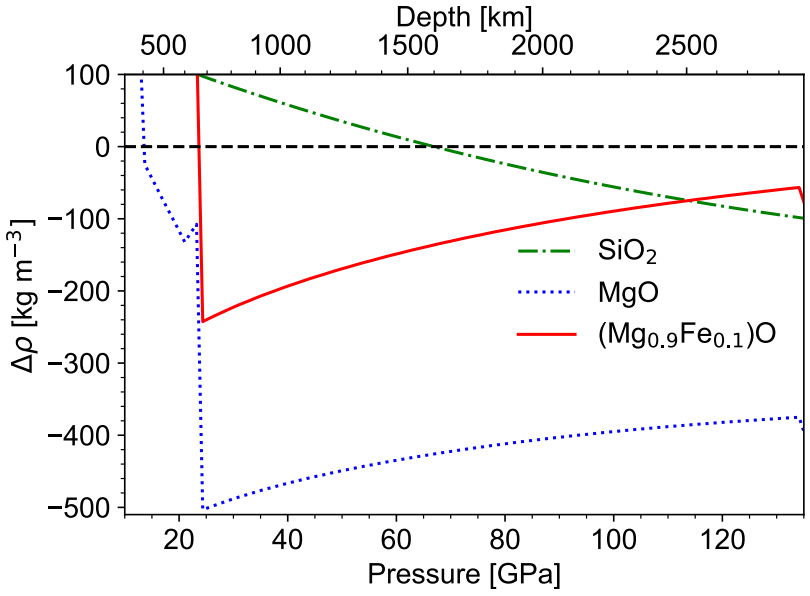

Supplementary Fig. 1 | Density difference ($\Delta\rho$) between exsolution and the PREM. $\Delta\rho$ is defined as $\Delta\rho = \rho_{\text{exsolution}} - \rho_{\text{PREM}}$. The results for SiO_2 is taken from ref.[50]. Densities of MgO periclase and $(Mg_{0.9}Fe_{0.1})O$ are calculated using the thermodynamic parameters in ref.[51] along the mantle geotherm[52]. $\Delta\rho = 0$ is also shown as a reference (black dashed line).

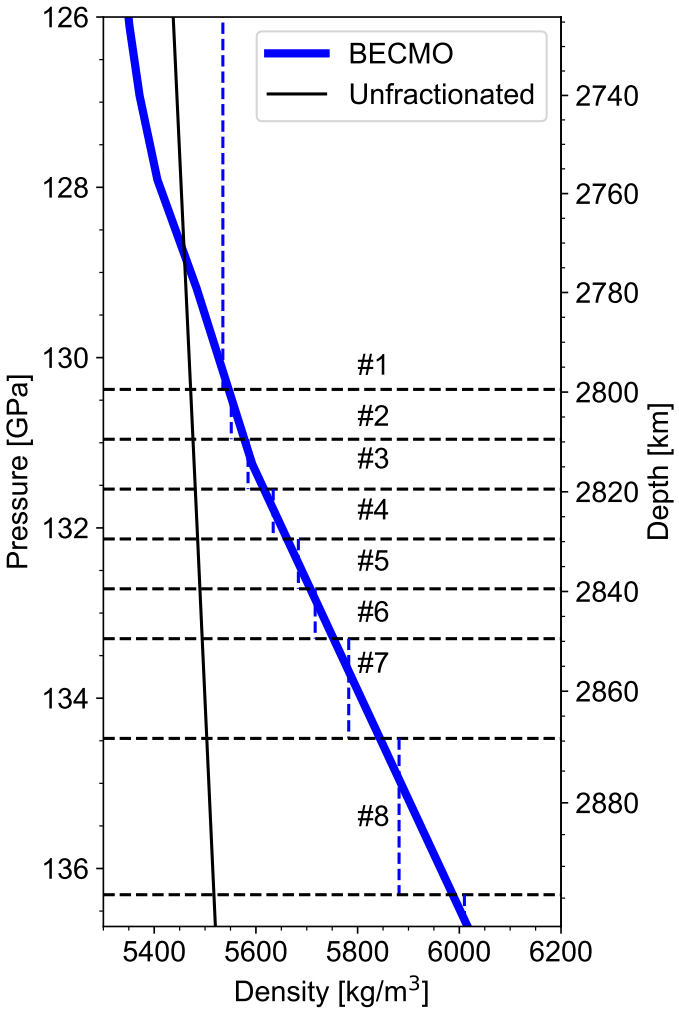

Supplementary Fig. 2| Density profile of the eight layers in the lowermost BECMO mantle. The solidified BECMO mantle (thick blue line) are subdivided into seven layers with the 8th layer added when convection reaches a quasi-steady state (see Method section for a detailed discussion) . Dashed lines represent the boundaries of these layers. Fractions of dense pile materials entrained from layers #1-8 are 61.02%, 63.69%, 1.36%, 0.28%, 0.04%, 0, 0.01%, 0, respectively. The density profile of the unfractionated mantle (black line) is also shown for comparison. The vertical blue dashed lines are the simplified discrete density for each layer adopted for geodynamic simulations.

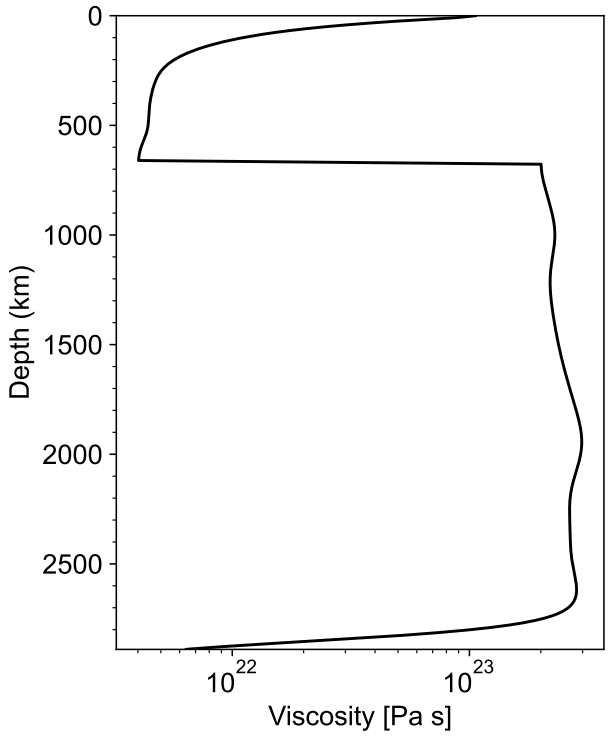

Supplementary Fig. 3 | Viscosity profile of the reference BECMO mantle after 4.5 Gyr.

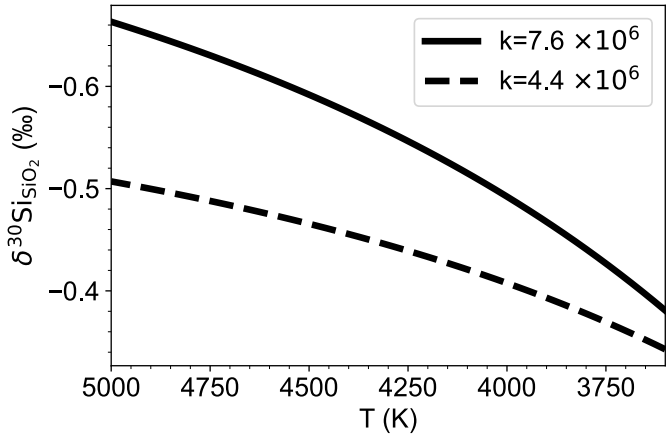

Supplementary Fig. 4 | Si isotopic composition of SiO_2 exsolution $\delta^{30}Si_{SiO2}$. The solid and dashed lines represent two different Si isotopic fractionation constants[34,35].

Supplementary Table 1. Mixing model inputs. The metal-oxide partitioning partition coefficient of W is assumed to be 1 and that of He 0.06 following ref. [9]. Values of dense piles are the average of composition of the solidified BECMO mantle at the depth range of 2770 km to 2810 km.

Component	Ambient mantle	Dense piles	Exsolution 1 $D_W = 1$ $D_{He} = 0.06$	Exsolution 2 $D_W = 10$ $D_{He} = 0.06$
^{4}He [cm^3 STP/g]	4.50E–06	1.87E–4	2.92E–04	2.92E–04
^{3}He [cm^3 STP/g]	5.00E–11	2.94E–8	4.71E–08	4.71E–08
^{3}He/^{4}He [R/R$_A$]	8	117	120	120
μ^{182}W	0	–119	–220	–220
W [ppb]	8	306	438	43.8

References

1 Lei, H. & He, J. Nucleation and Growth Kinetics of MgO in Molten Steel. *Journal of Materials Science & Technology* **28**, 642-646 (2012). https://doi.org:https://doi.org/10.1016/S1005-0302(12)60110-8

2 Parks, G. A. Surface and interfacial free energies of quartz. *Journal of Geophysical Research: Solid Earth* **89**, 3997-4008 (1984). https://doi.org:https://doi.org/10.1029/JB089iB06p03997

3 Klapczynski, V., Le Maux, D., Courtois, M., Bertrand, E. & Paillard, P. Surface tension measurements of liquid pure iron and 304L stainless steel under different gas mixtures. *Journal of Molecular Liquids* **350**, 118558 (2022). https://doi.org:https://doi.org/10.1016/j.molliq.2022.118558

4 Miyazaki, Y. & Korenaga, J. On the Timescale of Magma Ocean Solidification and Its Chemical Consequences: 1. Thermodynamic Database for Liquid at High Pressures. *Journal of Geophysical Research: Solid Earth* **124**, 3382-3398 (2019). https://doi.org:10.1029/2018JB016932

5 Monteux, J., Qaddah, B. & Andrault, D. Conditions for segregation of a crystal-rich layer within a convective magma ocean. *Journal of Geophysical Research: Planets* **128** (2023). https://doi.org:10.1029/2023JE007805

6 Li, Q., Xian, J.-W., Zhang, Y., Sun, T. & Vočadlo, L. Thermal Properties of Liquid Iron at Conditions of Planetary Cores. *Journal of Geophysical Research: Planets* **127**, e2021JE007015 (2022). https://doi.org:10.1029/2021JE007015

7 de Wijs, G. A. *et al.* The viscosity of liquid iron at the physical conditions of the Earth's core. *Nature* **392**, 805-807 (1998). https://doi.org:10.1038/33905

8 Labrosse, S., Hernlund, J. W. & Coltice, N. A crystallizing dense magma ocean at the base of the Earth's mantle. *Nature* **450**, 866-869 (2007). https://doi.org:10.1038/nature06355

9 Deng, J. & Du, Z. Primordial helium extracted from the Earth's core through magnesium oxide exsolution. *Nat Geosci* (2023). https://doi.org:10.1038/s41561-023-01182-7

10 Hirose, K. *et al.* Crystallization of silicon dioxide and compositional evolution of the Earth's core. *Nature* **543**, 4 (2017). https://doi.org:10.1038/nature21367

11 Chen, Y. & Zhang, Y. Olivine dissolution in basaltic melt. *Geochimica et Cosmochimica Acta* **72**, 4756-4777 (2008). https://doi.org:10.1016/j.gca.2008.07.014

12 Ghosh, D. B. & Karki, B. B. Transport properties of carbonated silicate melt at high pressure. *Science Advances* **3** (2017). https://doi.org:10.1126/sciadv.1701840

13 O'Rourke, J. G., Korenaga, J. & Stevenson, D. J. Thermal evolution of Earth with magnesium precipitation in the core. *Earth and Planetary Science Letters* **458**, 263-272 (2017). https://doi.org:10.1016/j.epsl.2016.10.057

14 Boukaré, C. E., Ricard, Y. & Fiquet, G. Thermodynamics of the MgO-FeO-SiO_2 system up to 140 GPa: Application to the crystallization of Earth's magma ocean. *Journal of Geophysical Research: Solid Earth* **120**, 2015JB011929 (2015). https://doi.org:10.1002/2015JB011929

15 Labrosse, S., Hernlund, J. W. & Hirose, K. in *The Early Earth* 123-142 (2015).

16 O'Rourke, J. G. Venus: A Thick Basal Magma Ocean May Exist Today. *Geophysical Research Letters* **47**, e2019GL086126 (2020). https://doi.org:https://doi.org/10.1029/2019GL086126

17 Caracas, R., Hirose, K., Nomura, R. & Ballmer, M. D. Melt–crystal density crossover in a deep magma ocean. *Earth and Planetary Science Letters* **516**, 202-211 (2019). https://doi.org:10.1016/j.epsl.2019.03.031

18 Yuan, Q. *et al.* Moon-forming impactor as a source of Earth's basal mantle anomalies. *Nature* **623**, 95-99 (2023). https://doi.org:10.1038/s41586-023-06589-1

19 Kato, C. *et al.* Melting in the FeOSiO2 system to deep lower-mantle pressures: Implications for subducted Banded Iron Formations. *Earth and Planetary Science Letters* **440**, 56-61 (2016). https://doi.org:https://doi.org/10.1016/j.epsl.2016.02.011

20 Ozawa, K., Anzai, M., Hirose, K., Sinmyo, R. & Tateno, S. Experimental Determination of Eutectic Liquid Compositions in the MgO-SiO2 System to the Lowermost Mantle Pressures. *Geophysical Research Letters* **45**, 9552-9558 (2018). https://doi.org:https://doi.org/10.1029/2018GL079313

21 Nabiei, F. *et al.* Investigating Magma Ocean Solidification on Earth Through Laser-Heated Diamond Anvil Cell Experiments. *Geophysical Research Letters* **48**, e2021GL092446 (2021). https://doi.org:10.1029/2021GL092446

22 Du, Z. & Lee, K. K. M. High-pressure melting of MgO from (Mg,Fe)O solid solutions. *Geophysical Research Letters* **41**, 8061-8066 (2014). https://doi.org:10.1002/2014GL061954

23 Deng, J. & Lee, K. K. M. Viscosity jump in the lower mantle inferred from melting curves of ferropericlase. *Nature Communications* **8** (2017). https://doi.org:10.1038/s41467-017-02263-z

24 Fu, S. *et al.* Melting behavior of the lower-mantle ferropericlase across the spin crossover: Implication for the ultra-low velocity zones at the lowermost mantle. *Earth and Planetary Science Letters* **503**, 1-9 (2018). https://doi.org:10.1016/j.epsl.2018.09.014

25 Ballmer, M. D., Lourenço, D. L., Hirose, K., Caracas, R. & Nomura, R. Reconciling magma-ocean crystallization models with the present-day structure of the Earth's mantle. *Geochemistry, Geophysics, Geosystems* **18**, 2785-2806 (2017). https://doi.org:10.1002/2017GC006917

26 Deng, J. Large-scale atomistic simulations of magnesium oxide exsolution driven by machine learning potentials: Implications for the early geodynamo. (2024). https://doi.org:10.17605/OSF.IO/MSRV4

27 Zhang, Z. *et al.* Free Energies of Fe-O-Si Ternary Liquids at High Temperatures and Pressures: Implications for the Evolution of the Earth's Core Composition. *Geophysical Research Letters* **49**, e2021GL096749 (2022). https://doi.org:10.1029/2021GL096749

28 Du, Z., Boujibar, A., Driscoll, P. & Fei, Y. Experimental Constraints on an MgO Exsolution-Driven Geodynamo. *Geophysical Research Letters* **46**, 7379-7385 (2019). https://doi.org:0.1029/2019GL083017

29 Deng, J. Large‐Scale Atomistic Simulations of Magnesium Oxide Exsolution Driven by Machine Learning Potentials: Implications for the Early Geodynamo. *Geophysical Research Letters* **51** (2024). https://doi.org:10.1029/2024gl109793

30 Du, Z. *et al.* Insufficient Energy From MgO Exsolution to Power Early Geodynamo. *Geophysical Research Letters* (2017). https://doi.org:10.1002/2017gl075283

31 Fischer, R. A. *et al.* High pressure metal–silicate partitioning of Ni, Co, V, Cr, Si, and O. *Geochimica et Cosmochimica Acta* **167**, 177-194 (2015). https://doi.org:10.1016/j.gca.2015.06.026

32 Rubie, D. C. *et al.* Accretion and differentiation of the terrestrial planets with implications for the compositions of early-formed Solar System bodies and accretion of water. *Icarus* **248**, 89-108 (2015). https://doi.org:10.1016/j.icarus.2014.10.015

33 Shahar, A. *et al.* High-temperature Si isotope fractionation between iron metal and silicate. *Geochimica et Cosmochimica Acta* **75**, 7688-7697 (2011). https://doi.org:10.1016/j.gca.2011.09.038

34 Hin, R. C., Fitoussi, C., Schmidt, M. W. & Bourdon, B. Experimental determination of the Si isotope fractionation factor between liquid metal and liquid silicate. *Earth and Planetary Science Letters* **387**, 55-66 (2014). https://doi.org:10.1016/j.epsl.2013.11.016

35 Moynier, F. *et al.* Metal-silicate silicon isotopic fractionation and the composition of the bulk Earth. *Earth and Planetary Science Letters* **549**, 116468 (2020). https://doi.org:10.1016/j.epsl.2020.116468

36 Ziegler, K., Young, E. D., Schauble, E. A. & Wasson, J. T. Metal–silicate silicon isotope fractionation in enstatite meteorites and constraints on Earth's core formation. *Earth and Planetary Science Letters* **295**, 487-496 (2010). https://doi.org:https://doi.org/10.1016/j.epsl.2010.04.030

37 Fitoussi, C., Bourdon, B., Kleine, T., Oberli, F. & Reynolds, B. C. Si isotope systematics of meteorites and terrestrial peridotites: implications for Mg/Si fractionation in the solar nebula and for Si in the Earth's core. *Earth and Planetary Science Letters* **287**, 77-85 (2009). https://doi.org:10.1016/j.epsl.2009.07.038

38 Savage, P. S., Armytage, R. M. G., Georg, R. B. & Halliday, A. N. High temperature silicon isotope geochemistry. *Lithos* **190-191**, 500-519 (2014). https://doi.org:https://doi.org/10.1016/j.lithos.2014.01.003

39 Mundl, A. *et al.* Tungsten-182 heterogeneity in modern ocean island basalts. *Science* **356**, 66-69 (2017). https://doi.org:10.1126/science.aal4179

40 White, W. Probing the Earth's Deep Interior Through Geochemistry. *Geochemical Perspectives*, 95-251 (2015). https://doi.org:10.7185/geochempersp.4.2

41 Mabry, J., Lan, T., Burnard, P. & Marty, B. High-precision helium isotope measurements in air. *Journal of Analytical Atomic Spectrometry* **28**, 1903-1910 (2013). https://doi.org:10.1039/C3JA50155H

42 Rizo, H. *et al.* ^{182}W evidence for core-mantle interaction in the source of mantle plumes. *Geochemical Perspectives Letters* **11**, 6-11 (2019). https://doi.org:10.7185/geochemlet.1917

43 Huang, D., Siebert, J. & Badro, J. High pressure partitioning behavior of Mo and W and late sulfur delivery during Earth's core formation. *Geochimica et Cosmochimica Acta* **310**, 19-31 (2021). https://doi.org:https://doi.org/10.1016/j.gca.2021.06.031

44 Mahaffy, P. R., Donahue, T. M., Atreya, S. K., Owen, T. C. & Niemann, H. B. Galileo Probe Measurements of D/H and ^{3}He/^{4}He in Jupiter's Atmosphere. *Space Sci Rev* **84**, 251-263 (1998). https://doi.org:10.1023/A:1005091806594

45 McDonough, W. F. in *Treatise on Geochemistry* (eds Heinrich D. Holland & Karl K. Turekian) 547-568 (Pergamon, 2003).

46 Li, Y., Vočadlo, L., Ballentine, C. & Brodholt, J. P. Primitive noble gases sampled from ocean island basalts cannot be from the Earth's core. *Nature Communications* **13**, 3770 (2022). https://doi.org:10.1038/s41467-022-31588-7

47 Mundl-Petermeier, A. *et al.* Anomalous ^{182}W in high ^{3}He/^{4}He Ocean Island Basalts: Fingerprints of Earth's core? *Geochimica et Cosmochimica Acta* (2020). https://doi.org:10.1016/j.gca.2019.12.020

48 Peters, D., Rizo, H., O'Neil, J., Hamelin, C. & Shirey, S. B. Comparative 142Nd and 182W study of MORBs and the 4.5 Gyr evolution of the upper mantle. *Geochemical Perspectives Letters* **29**, 51-56 (2024). https://doi.org:https://doi.org/10.7185/geochemlet.2412

49 Peters, D. *et al.* Tungsten in the mantle constrained by continental lithospheric peridotites: Less incompatible and more abundant. *Geochimica et Cosmochimica Acta* **351**, 167-180 (2023). https://doi.org:https://doi.org/10.1016/j.gca.2023.04.016

50 Helffrich, G., Ballmer, M. D. & Hirose, K. Core-Exsolved SiO_2 Dispersal in the Earth's Mantle. *Journal of Geophysical Research: Solid Earth* **123**, 176-188 (2018). https://doi.org:10.1002/2017JB014865

51 Stixrude, L. & Lithgow-Bertelloni, C. Thermodynamics of mantle minerals - II. Phase equilibria. *Geophys J Int* **184**, 1180-1213 (2011). https://doi.org:10.1111/j.1365-246X.2010.04890.x

52 Anderson, O. The power balance at the core–mantle boundary. *Physics of the Earth and Planetary Interiors* **131**, 1-17 (2002). https://doi.org:10.1016/S0031-9201(02)00009-2